Advanced Noise and Interference Suppression Techniques for Pulsed Light Detection and Ranging Sensors in Automotive Urban-Driving Applications

Sadra Tafaghodi Jami[a,b], Ali Fotowat-Ahmady[a,*], and Jie Yuan[b]

a. Department of Electrical Engineering, Sharif University of Technology, Tehran, Iran
b. Department of Electronic and Computer Engineering, The Hong Kong University of Science and Technology, Hong Kong
[*]Corresponding author: afotowat@sharif.edu (Ali Fotowat-Ahmady)

Abstract

This paper explores advanced techniques for noise and interference suppression in pulsed light detection and ranging (LiDAR) sensors, with a focus on automotive urban-driving applications. In complex urban scenarios, LiDAR performance is challenged by strong ambient light, dominated by sunlight, and interference from nearby sensors. To address these issues, circuit- and system-level strategies are developed to enhance photon detection reliability, mitigate background noise, and suppress inter-LiDAR interference while maintaining high timing precision and power efficiency. The proposed methods are evaluated through theoretical analysis, simulations, and experimental measurements using a custom-fabricated single-photon avalanche diode (SPAD)-based sensor chip in 180-nm HV CMOS technology. Results demonstrate significant enhancements in noise and interference resistance, ranging accuracy, and robustness under illumination levels typical of daytime urban environments. The system enables 20-fps depth imaging at distances up to 34 m under 79-klux background illumination, and accurate single-point target detection up to 100 m under 103-klux background illumination. These advances pave the way for reliable and scalable LiDAR systems for autonomous and assisted driving in dynamic urban settings.

Keywords: Pulsed LiDAR; Single-Photon Avalanche Diode (SPAD); Direct Time-of-Flight (d-ToF); Background Noise Suppression; Inter-LiDAR Interference; Automotive; Urban Driving

1. Introduction

Autonomous and assisted driving systems depend on high-resolution 3D perception for safe operation in complex urban environments. Pulsed LiDAR has become a key technology for real-time depth sensing, providing accurate ranging and robust spatial mapping across diverse driving conditions (Niclass et al. [1] and Yoshioka et al. [2]). It must therefore achieve high accuracy, low latency, and strong resilience to ambient light and inter-LiDAR interference in dense traffic scenarios (Li and Ibanez-Guzman [3]).

Single-photon avalanche diode (SPAD)-based direct time-of-flight (d-ToF) sensors are a leading solution for high-resolution depth sensing in pulsed LiDARs (Morrison et al. [4] and Jami et al. [5]). Their single-photon sensitivity and picosecond timing precision enable long-range, high-speed applications such as automotive perception and autonomous navigation (Villa et al. [6]). Depth estimation relies on accurate photon arrival-time measurement of short laser pulses. However, SPADs cannot inherently distinguish between signal and non-signal photons, as both trigger identical avalanche events (Chen et al. [7]). In urban environments with strong sunlight, reflective surfaces, and multiple LiDAR sources, this results in degraded SNR, depth accuracy, and reliability. Therefore, effective noise and interference suppression is a key requirement for SPAD-based d-ToF automotive LiDARs.

Recent SPAD-based LiDAR advances have introduced noise and interference suppression techniques, but performance remains constrained under realistic automotive conditions. Time-correlated single-photon counting (TCSPC) methods (Incoronato et al. [8] and Feng et al. [9]) use temporal gating and histogram-based processing to suppress noise and enhance signal discrimination. In TCSPC, all detected photons (signal, noise, and interference), are accumulated into a histogram, whose peak corresponds to the correct ToF.

Background noise in SPAD-based d-ToF LiDARs can be modeled as (Padmanabhan et al. [10])

$$N_{\mathrm{BGL}} = \frac{I_{\mathrm{vis}} \cdot A_{\mathrm{lens}} \cdot T_{\mathrm{vis}} \cdot \rho \cdot \lambda_{\mathrm{vis}} \cdot \mathrm{FF} \cdot \mathrm{PDP} \cdot T_{\mathrm{int}}}{N_{\mathrm{pix}} \cdot h \cdot c}, \tag{1}$$

where N_{BGL} is the number of background-light events, I_{vis} is visible light irradiance, A_{lens} is receiver lens area, T_{vis} is visible light transmission, ρ is target reflectivity, λ_{vis} is the visible light wavelength, FF is pixel fill factor, PDP is photon detection probability of the SPADs, T_{int} is histogram integration time, N_{pix} is pixel count, and h and c are Planck's constant and speed of light, respectively. Since sunlight dominates daytime noise, background light is assumed to be in the visible range. Under typical daylight conditions (~100 klux or 1 kW/m^2 sunlight irradiance), and assuming a 1-inch diameter receiver lens, 20% target reflectivity, 550-nm average visible wavelength, FF = 14%, PDP = 4%, T_{int} = 10 ms, and a 68×40 pixel array, the number of background noise events is calculated as 5769. An optical bandpass filter (BPF) with an optical density (OD) of 6 (transmission of 10^{-6}) is also assumed in front of the sensor to provide partial suppression for visible light.

The number of signal events is estimated by (Padmanabhan et al. [10])

$$N_{\text{sig}} = \frac{P_{\text{laser}} \cdot \lambda_{\text{laser}} \cdot T_{\text{PW}} \cdot \rho \cdot A_{\text{lens}} \cdot \text{FF} \cdot \text{PDP} \cdot T_{\text{int}}}{N_{\text{pix}} \cdot h \cdot c \cdot \pi \cdot R^2 \cdot e^{2\alpha R} \cdot T_{\text{cycle}}}, \quad (2)$$

where P_{laser} is laser peak power, λ_{laser} is laser wavelength, T_{PW} is laser pulse width, R is target range, α is attenuation factor of light in the air, and T_{cycle} is duration of one laser cycle. With typical values of P_{laser} = 50 W, λ_{laser} = 905 nm, T_{PW} = 10 ns, α = 0.1 km^{-1}, and T_{cycle} = 1 µs (translating to 150-m maximum range), at 100-m range, the number of detected signal events is calculated as 148.

These conditions yield an SNR of approximately -32 dB. Although histogram processing distributes noise over time and improves SNR, it remains insufficient for reliable long-range detection in bright daylight. Moreover, interference from other LiDARs in urban environments further degrades performance, underscoring the need for more advanced noise and interference suppression techniques in automotive applications.

Automotive LiDAR also demands high frame rates and low latency. Real-time urban perception requires tens of frames per second and rapid photon processing across large SPAD arrays (Dai et al. [11]). Thus, suppression techniques must provide strong noise and interference resilience without reducing frame rate, an ongoing challenge for current architectures.

To mitigate mutual interference, Kashmiri et al. [12] proposed pulse compression via burst transmission with matched filtering, while pulse-position modulation (PPM) schemes (Grollius et al. [13] and Zhu et al. [14]) encode temporal or coded signatures into pulses to distinguish returns from different LiDARs. Seo et al. [15] introduced dividing each pulse into two sub-pulses with a temporal offset for correlation-based interference rejection. These methods improve resilience but reduce maximum detection range due to eye-safety limits, and additional histogramming steps can lower frame rate. Range-gating techniques (Ruokamo et al. [16] and Padmanabhan et al. [17]) suppress ambient light and out-of-window interference, but require sweeping or adapting the gate in dynamic scenarios, degrading frame rate or SNR. Thus, traditional methods often trade photon efficiency, temporal precision, or real-time operation for interference suppression, limiting their use in high-speed automotive LiDAR.

In this work, we explore and experimentally validate novel noise and interference suppression techniques for SPAD-based d-ToF LiDAR that maintain high frame rate and ranging accuracy while rejecting ambient noise and mutual interference. Using theory, simulations, and measurements from a custom-fabricated SPAD sensor, we show substantial improvements in SNR, depth precision, and robustness under urban automotive conditions.

The remainder of this paper is organized as follows. Section 2 introduces the proposed suppression techniques and their implementation within the LiDAR architecture, together with corresponding theoretical analysis and simulation results. Section 3 presents experimental results, with detailed discussion on the results provided in Section 4. Finally, Section 5 concludes the paper.

2. Proposed Methods

This section introduces three novel techniques developed to enhance suppression of non-signal detections, including background noise and interference, in SPAD-based d-ToF LiDAR sensors: time-coded TCSPC, adaptive coincidence detection, and pixel-wise range gating. Each method targets specific limitations of existing suppression strategies while maintaining high photon efficiency and real-time operation.

2.1 Time-Coded TCSPC

TCSPC is widely used in SPAD-based d-ToF sensors for reconstructing photon arrivals by accumulating histograms over multiple cycles. However, conventional implementations are susceptible to cross-sensor interference, which can introduce false peaks in the histogram, sometimes surpassing the true signal peak in amplitude. To mitigate this, we propose a time-coded TCSPC technique that applies a controlled temporal modulation to the laser repetition rate. The modulation amplitude is kept much smaller than the base repetition rate, allowing effective discrimination between genuine and interfering signals. Originally developed in our earlier work (Dabidian et al. [18]) for linear-mode LiDAR, this approach enables robust signal identification without compromising range or frame rate in controlled environments. Here, we extend and adapt the method for SPAD-based detection, implementing it on a custom-fabricated SPAD chip to assess its performance under realistic conditions.

As illustrated in Figure 1, the pseudo-random modulation applied to the laser repetition rate causes a gradual temporal drift in the transmitted laser pulses with respect to fixed timing references (shown in red). The SPAD sensor, however, operates according to these fixed references, and the time-to-digital converter (TDC) measures photon event times relative to them. A subsequent post-processing step, performed either on-chip or on an FPGA, decodes the TDC output data to reconstruct event histograms based on the decoded timing. In fact, the transmitted laser pulses that follow the known pseudo-random pattern are reconstructed in the final histogram,

whereas the non-signal returns (including noise and interference) are distributed across the histogram according to the coding pattern, effectively suppressing their influence. Since the codes can be selected randomly from a large pool of available codes, even if some LiDAR sensors in the environment use the exact same coding scheme as our sensor, the actual selected codes per imaging frame is most likely different. For This reason, the proposed method can effectively suppress interference signals from multiple interfering sources.

Compared to conventional approaches, this method offers enhanced performance for high-speed 3D depth imaging under realistic urban-driving conditions. As depicted in Figure 2, each imaging frame consists of M code repetitions, followed by a decoding stage. During each code repetition, all available codes are utilized, resulting in 2^n possible modulation codes for an n-bit sequence. Each code repetition thus includes 2^n laser pulses, which are modulated according to the n -bit pseudo-random sequence. In subsequent repetitions, different modulation codes are used, producing a continuous drift of transmitted pulses over the imaging frame that spreads potential interference signals. A key advantage of this scheme is that, within each measurement cycle (i.e., the interval between two consecutive timing references), only one laser pulse is transmitted. Since eye-safety limits total laser energy per cycle, and each laser pulse width is typically set by the detection circuitry, the use of only one laser pulse per measurement cycle enables the laser source to operate at a higher peak power compared to multi-pulse schemes. Increasing the transmitted peak power in turns increases the received optical power from an object at a given distance, thereby extending the maximum measurable range of the LiDAR sensor. Moreover, since the entire coding and decoding process is completed within a single imaging frame, the sensor's frame rate remains unaffected. Background noise is reduced by a factor of $M\times 2^n$ through standard TCSPC averaging, while interference signals are further suppressed by a factor of 2^n due to the temporal coding.

To evaluate the effectiveness of this technique, we consider a SPAD-based d-ToF LiDAR employing TCSPC with pseudo-randomly modulated laser repetition rate. A multi-target scenario is assumed, consisting of N_t targets located at different distances. Before decoding, accumulated events form the histogram

$$h(t) = h_{\text{sig}}(t) + h_{\text{BGL}}(t) + h_{\text{int}}(t), \tag{3}$$

where $h_{\text{sig}}(t)$, $h_{\text{BGL}}(t)$, and $h_{\text{int}}(t)$ denote signal, background noise, and interference contributions, respectively. The applied modulation introduces temporal shifts dT_k into the transmitted pulses, leading to the following expression for signal histogram:

$$h_{\text{sig}}(t) = \sum_{k=1}^{N_p} \sum_{m=1}^{N_t} A_m \cdot \delta\left(t - \left(\text{ToF}_m + dT_k\right)\right), \tag{4}$$

where N_p represents the total number of pulses, A_m is signal amplitude, and $\text{ToF}_m = 2R_m/c$ is the time-of-flight (ToF) corresponding to m-th target at distance R_m. Assuming uniform background illumination, noise histogram can be modeled as

$$h_{\text{BGL}}(t) = N_p \cdot r_{\text{BGL}}, \tag{5}$$

where r_{BGL} denotes background photon count rate per histogram bin. For worst-case interference scenario, namely, an external source operating at the same base repetition rate as the main laser, the interference component is modeled as

$$h_{\text{int}}(t) = \sum_{k=1}^{N_p} A_i \cdot \delta\left(t - \text{ToF}_i\right), \tag{6}$$

where A_i and ToF_i represent the amplitude and ToF of the interfering signal, respectively. To reconstruct the signal, a matched-filter decoding process is applied by shifting each histogram slice by dT_k, expressed as

$$h_{\text{MF}}(t) = \sum_{k=1}^{N_p} h\left(t + dT_k\right), \tag{7}$$

which yields the following components:

$$h_{\text{dec,sig}}(t) = N_p \sum_{m=1}^{N_t} A_m \cdot \delta\left(t - \text{ToF}_m\right), \tag{8}$$

$$h_{\text{dec,BGL}}(t) = N_p \cdot r_{BGL}, \tag{9}$$

$$h_{\text{dec,int}}(t) = \sum_{k=1}^{N_p} A_i \cdot \delta\left(t - \left(\text{ToF}_i - dT_k\right)\right). \tag{10}$$

Due to n-bit temporal coding, the interference term $h_{\text{dec,int}}(t)$ is effectively distributed across 2^n histogram bins, reducing its per-bin strength by the same factor.

To quantify performance, the signal-to-noise-and-interference ratio (SNIR) parameter is defined, taking into account simultaneous suppression of noise and interference. The SNIR for m-th target can be expressed as

$$\text{SNIR}_m = \frac{A_m^{\,2}}{\left(\frac{A_i}{2^n} + r_{\text{BGL}}\right)^2}. \tag{11}$$

This relationship demonstrates that signal contributions from true targets remain coherently reinforced after decoding, while interference signals are dispersed and background noise is statistically averaged. Since r_{BGL} is defined per histogram bin, increasing histogram resolution further enhances SNIR.

Simulation results of time-coded TCSPC using 4-bit modulation are shown in Figure 3. The results demonstrate that strong interference signal is distributed across 16 histogram bins through standard TCSPC, resulting in an approximate 11.2-dB improvement in histogram SNIR. Moreover, under controlled illumination conditions, the increase in histogram background level caused by interference spreading can be compensated based on the known modulation pattern, providing additional improvement of approximately 6.8 dB in SNIR.

Overall, time-coded TCSPC preserves both the maximum measurable range and imaging frame rate of SPAD-based d-ToF LiDAR systems, while providing substantial suppression of non-signal events in the histogram. Moreover, since TCSPC typically employs a large number of pulses, time-coding patterns can be designed to remain orthogonal across multiple LiDAR units, enabling scalable and interference-resilient operation in dense automotive environments.

2.2 Adaptive Coincidence Detection

SPAD-based LiDARs frequently operate under photon-starved conditions, where random ambient photons can induce false avalanche events. Traditional coincidence detection approaches, such as those proposed by Manuzzato et al. [19] and Hu et al. [20], address this by validating events only when two or more SPADs within a defined neighborhood fire within a short temporal window, typically matching the pulse width. However, they rely on fixed thresholds, which may not perform optimally under varying conditions.

The proposed adaptive coincidence detection technique dynamically adjusts the coincidence threshold according to the high-voltage supply applied to SPADs. This approach is particularly effective in compensating for variations in the SPADs' dark count rate (DCR), which is strongly dependent on supply voltage. Even small increase in supply voltage can cause substantial rise in DCR, leading to unreliable ToF measurements. By automatically increasing the detection threshold as supply voltage rises, this method effectively suppresses noise at higher voltages and maintains stable sensor operation across wider voltage range.

Figure 4 depicts conceptual operation and circuit-level implementation of adaptive coincidence detection. It operates based on three distinct thresholds, determining whether one, two, or three detections in each macro-pixel of four neighboring SPADs in a time window matching the laser pulse width are required for valid event detection. The threshold is then set by comparing the supply voltage by two voltages "VSPAD_TH_HI" and "VSPAD_TH_LO", and setting the threshold accordingly. These voltages can be controlled to account for different background illumination conditions. In noisy environments, they are lowered to enable coincidence detection at lower voltages, providing stronger noise suppression, and vice versa.

This adaptive approach offers two main advantages. First, it effectively rejects background noise, resulting in significantly improved SNR. Second, it broadens the sensor's operational voltage range, ensuring reliable performance across diverse illumination conditions. In contrast, conventional fixed-threshold methods suffer from missed detections at low voltages or excessive noise at high voltages due to increased DCR and ambient light. The adaptive technique mitigates these issues by maintaining high SNR and stable operation across wider voltage range. Furthermore, it can be implemented efficiently at the array or subarray level with minimal additional circuitry, making it highly scalable for large SPAD arrays. When integrated with TCSPC, the system achieves enhanced robustness by cross-validating events both spatially and temporally.

2.3 Pixel-Wise Range Gating

Range gating is a technique used to restrict the detection range of a sensor to a narrow time window instead of the full measurement range, and it is a known method for improving SNR in d-ToF LiDARs. By observing a limited temporal window, non-signal events, such as those caused by ambient noise or interference, that fall outside this window are automatically excluded, while valid signal events within the window are captured. However, conventional methods employ fixed windows shared across the entire pixel array. This lack of flexibility reduces performance in dynamic scenes containing objects at different depths. To compensate, the window must typically be swept across the full measurement range per frame, which substantially lowers frame rate.

The proposed approach introduces a locally adaptive gating mechanism, where each macro-pixel, comprising four neighboring SPADs used for coincidence detection, maintains an independently-controlled gating window. The window parameters are dynamically adjusted based on prior depth estimates by local histogram statistics. By continuously updating these parameters

in real time, the system preserves sensitivity to relevant depth ranges while effectively suppressing out-of-range noise and interference photons, resulting in improved adaptability and overall system performance.

Figure 5 illustrates the conceptual operation of pixel-wise range gating. Unlike conventional methods, the window is individually defined per pixel based on its coarse ToF estimate obtained during a preliminary pre-imaging stage, corresponding to laser pre-shots 1–*M* shown in the figure. Since this stage operates at a low timing resolution, it can be completed rapidly. During the subsequent main imaging phase, corresponding to laser shots 1–*N*, per-pixel gating window is applied to acquire the fine depth image. Only events that fall within the designated gating window for each pixel are accumulated in the histogram, while those outside the window are discarded. This selective accumulation effectively suppresses noise events, particularly those associated with pile-up distortion (Gyongy et al. [21]), while preserving the true signal counts. Consequently, histogram peak forms more quickly relative to background noise, resulting in significant improvement in SNR. Overall, pixel-wise range gating enables high-resolution depth imaging at increased frame rates. It enhances image quality and extends sensor's maximum measurable range while simultaneously reducing on-chip memory requirements for histogram storage.

Circuit-level implementation of this technique is illustrated in Figure 6. During pre-imaging phase, each pixel generates a low-resolution histogram using the coarse ToF data "C_TOF" obtained from TDC. Once this phase is completed, a gating window indicator "RG_WIN" is determined for every pixel based on its histogram profile and stored in an on-chip memory. In the prototype sensor developed for this work, including a 68×40 pixel array, this requires about 1-kB on-chip memory. During subsequent measurement cycles, this stored information remains constant. When an event is detected, the pixel address is used to retrieve corresponding RG_WIN via multiplexing. The selected window indicator defines gating thresholds "RG_TH_LO" and "RG_TH_HI" that are then compared against C_TOF. Output signal "RG_VALID" acts as a validation flag, indicating whether the detected event falls within the appropriate window for that pixel. The entire pixel-wise range gating function can be disabled by pulling "RG_EN" low. A new pre-imaging phase is initiated at the beginning of each frame to refresh the memory with updated per-pixel window information. The details of pixel addressing and ToF measurement performed by the TDC are beyond the scope of this paper and are therefore not discussed here. In the implemented prototype, gating logic block shown in Figure 6 follows the configuration

summarized in Table 1, where eight distinct windows are employed to cover depth measurements up to 60-m range.

A system-level simulation is presented in Figure 7, where background noise is modeled using Poisson distribution (Tontini et al. [22]). Pile-up distortion is also included, assuming a limited throughput of three events/cycle, consistent with the prototype sensor's characteristics. Target return signal is positioned at 15.2 m. Results demonstrate that range gating substantially improves histogram SNR while effectively mitigating pile-up distortion. Furthermore, since gating window is determined through a low-resolution, fast histogramming stage within each frame, the process can be performed on a per-pixel basis without the need for gate sweeping, thus preserving high frame rate.

3. Measurement Results

The proposed suppression techniques were experimentally validated using a SPAD-based d-ToF sensor chip fabricated in 180-nm HV CMOS. The chip features an array of 68×40 macro-pixels, each consisting of four SPADs configured for coincidence detection. The coincidence threshold is dynamically controlled through SPADs' supply voltage, enabling adaptive coincidence detection described earlier. Eight on-chip TDC blocks are integrated, each responsible for a 17×20-pixel region, providing both coarse and fine ToF measurements with 10-ns and 156.25-ps resolutions, respectively. Coarse timing data is subsequently used to implement pixel-wise range gating. When a detected event passes range-gating validation based on its coarse ToF, corresponding fine ToF value is accepted as the high-resolution timing measurement; otherwise, it is discarded. Final ToF data is then transmitted to a Kintex-7 FPGA on a Digilent Genesys 2 board for further processing.

3.1 Measurement Setup

The fabricated sensor chip was evaluated within a LiDAR setup, as shown in Figure 8. The system employs a 905-nm pulsed laser diode (SPL TL90AT08) as the illumination source, driven by a high-power driver (EPC9126). A 1-inch diameter, 25-mm focal length lens (LA1951-B) is positioned in front of the sensor, forming the scene image. This optical configuration provides a field-of-view (FoV) of approximately 8.5°×7.5°. To suppress ambient illumination, a 1-inch diameter optical BPF centered at 905 nm with a 25-nm linewidth (FBH905-25) is placed between

the receiver lens and the sensor. The filter provides an OD of about 5.9 in the visible range, corresponding to an attenuation factor of roughly 8×10^6. For single-point measurements (telemetry), a 1-inch diameter, 30-mm focal length lens (LA1805-B) is placed in front of the laser to collimate the beam. For imaging applications, this lens is removed to provide flash illumination.

The driver operates the laser at a peak power of 50 W, with a 100-kHz repetition rate and 10-ns pulse width. Two voltages are generated by the power supply: a 30-V supply used to power the laser driver and SPADs, and an 8-V supply dedicated to the logic circuitry. The 30-V supply is further regulated by a variable low-dropout (LDO) regulator to provide adjustable supply of 20–30 V for the SPADs. Similarly, the 8-V supply is stepped down to 1.8 V, 3.3 V, and 5 V using three additional LDO regulators to power the logic circuits within the driver and sensor chip.

The FPGA controls LiDAR operation by providing clock and control signals. The START_MOD signal, modulated according to the coding scheme described earlier, triggers the laser. The START signal, an unmodulated version of START_MOD, marks the beginning of each cycle and is sent to the sensor chip. After each cycle, the RO_START signal initiates the readout. Two additional clocks "TDC_CLK" and "RO_CLK", with frequencies of 100 MHz and 10 MHz respectively, drive the TDC and the readout circuitry on the sensor. The resulting output data "DATA_OUT" is then transferred to the FPGA at a 10-MHz rate for further processing.

To emulate interference during measurements, a second laser, identical to the primary laser, is used and driven by a separate driver triggered by START. Its power is adjustable through the driver, while its ToF can be controlled by varying its distance from the sensor.

The implemented LiDAR was evaluated under three test conditions: indoor environment with 800-lux background illumination and a maximum range of 5.2 m; outdoor environment with 79-klux illumination and a 54-m maximum range; and another outdoor environment with 103-klux illumination and a 100-m maximum range. These test conditions are hereafter referred to as SETUP1, SETUP2, and SETUP3, respectively. SETUP2 is designed to evaluate performance under mid-range conditions, representative of dense urban environments that require fast and accurate imaging. In this setup, flash illumination is employed with shorter integration times to emulate high-speed imaging. In contrast, SETUP3 targets long-range performance, where imaging is typically unnecessary. Thus, the sensor operates in single-point (telemetry) mode, emulating range-finding operation under long-distance, high background noise conditions.

Physical configuration of the indoor setup “SETUP1” along with die micrograph of the sensor chip is illustrated in Figure 9, and the outdoor setups “SETUP2” and “SETUP3” are shown in Figure 10.

3.2 SETUP1 Measurement Results

Owing to the low background noise and strong signal reflections in this setup, the SNR is inherently high, making it suitable primarily for validating interference suppression. A 4-bit pseudo-random modulation is applied to the laser repetition rate according to the previously described time-coded TCSPC. To emulate a realistic multi-target scenario, two targets are positioned at distances of 4.35 m and 5.05 m. The receiver lens is removed so that all pixels capture the entire scene, including both targets and the interference. The interference directly illuminates the sensor, rather than reflecting from the targets, with its power adjusted by changing its distance (due to beam divergence) and its ToF controlled via its trigger pulse. The coding time step is set to the minimum value of 156.25 ps (matching the sensor's resolution) in this setup.

The TCSPC decoding is implemented on the FPGA. For this test, TDC data is transferred off-chip to the FPGA with a limited throughput of three events/cycle for each half-column (20 pixels). The FPGA performs time-coded TCSPC decoding and generates the final histograms, in which the strong interference signal is effectively spread across multiple bins.

Figure 11 presents measurement results with and without coding. Given the short range, only the 6-bit fine ToF data from the TDC with 156.25-ps resolution is used, corresponding to a 10-ns (1.5-m) window. Thus, the histograms cover the window of 3.9–5.4 m, clearly showing both targets at 4.35 m and 5.05 m, along with the strong interference. Measurements show an interference suppression of 15.85 dB through its spreading across 16 consecutive bins, leading to the proper detection of both targets with good accuracy.

To evaluate the method in a realistic high-resolution, fast-imaging scenario, the sensor chip was used to capture a 68×40-pixel depth image of a scene under strong interference. In this setup, the receiver lens is mounted to form a focused image, while the interference illuminates the same scene with a peak power approximately 20% higher than that of the main laser, producing reflections back toward the sensor. For each frame, 1000 pulses are transmitted, and detected events are accumulated into per-pixel histograms to compute the corresponding ToF values. With a 100-kHz repetition rate, transmitting 1000 pulses requires 10 ms, followed by about 1.5 ms of

post-processing on the FPGA (including histogramming and decoding). This yields an effective imaging frame rate of 87 fps. Since time-coded TCSPC is implemented within the regular TCSPC processing, this high frame rate is achieved while providing proper interference suppression in 3D imaging. Therefore, the proposed method does not limit the sensor's frame rate.

The results, shown in Figure 12, demonstrate successful high-speed imaging with a depth resolution of 2.34 cm, while effectively suppressing the strong interference signal.

The adaptive coincidence detection technique is also evaluated in this setup. Because the background illumination is relatively low, the coincidence threshold is adjusted primarily based on the DCR of the SPADs, which depends on the SPADs' supply voltage. Figure 13 shows the measured histograms of combined coarse and fine ToF data (with 156.25-ps resolution) from a single pixel at supply voltages of 22.5 V and 23 V, with the adaptive coincidence detection mechanism disabled. An object is placed at 4.5-m range, acting as the main target. The results indicate that the sensor is highly sensitive to voltage variations, a 0.5-V increase in supply voltage causes a significant rise in DCR and pronounced pile-up distortion due to the sensor's limited throughput, rendering the ToF measurement unreliable. When the adaptive coincidence detection is enabled, the corresponding histograms at 22.5 V and 26.5 V (also shown in Figure 13) demonstrate effective noise suppression at higher voltages by adjusting the coincidence detection threshold according to supply voltage. At lower voltages, however, the coincidence detection threshold is lowered to capture more events. Meanwhile, at lower voltages, the coincidence detection threshold is lowered so that no suppression is provided in the bottom-left subplot of Figure 13. This allows the sensor to maintain stable operation across an extended 4-V supply range, significantly improving robustness against high voltage-induced noise. Ideally, the optimum values for supply voltage thresholds used in adaptive coincidence detection (VSPAD_TH_LO and VSPAD_TH_HI in Figure 4) are chosen based on the PDP and DCR characteristics of the SPADs versus supply voltage, and the expected background illumination level in the environment. However, in the prototype sensor presented in this paper, these values are simply determined by sweeping the supply voltage and capturing the histograms for different coincidence detection levels. For SETUP1, threshold levels of 22.8 V and 24.5 V have been found to give the best SNR performance through the supply sweep and histogram SNR measurement.

Due to the limited maximum range of this setup, the range-gating mechanism is not evaluated here and is instead validated in the other experimental setups.

3.3 SETUP2 Measurement Results

This setup is designed to evaluate performance under mid-range, high-noise conditions, where fast and accurate imaging is critical. The background illumination is considerably higher (79 klux), making suppression techniques essential for reliable operation. Time-coded TCSPC is tested using a 4-bit pseudo-random modulation scheme, similar to the previous setup. However, to enable flash imaging, the receiver lens is mounted in front of the sensor. The interference operates with a peak power about 20% higher than the main laser, illuminating the same scene and reflecting back to the sensor. The target is placed at 20-m distance, with the interference triggered 20 ns after the main laser. A 5-ns coding time step is used to clearly demonstrate interference spreading in the histogram.

Figure 14 shows the measurement results obtained with and without coding. For longer-range measurements, both the 8-bit coarse and 6-bit fine ToF data from the TDC, corresponding to 10-ns and 156.25-ps resolutions, are combined to form a single histogram with 16384 bins and 156.25-ps resolution (equivalent to 2.34-cm range resolution). Results demonstrate 16.3-dB interference suppression achieved by spreading the interference across 16 bins with 75-cm separation, consistent with the 5-ns time step used in the coding pattern. This enables accurate detection of the main target. Additionally, while high background illumination introduces pile-up in the histogram, the applied coding successfully reduces the interference below the pile-up level.

Due to high background illumination in this setup, the supply voltage thresholds for adaptive coincidence detection are slightly reduced to 22.5 V and 24 V. Consequently, coincidence threshold remains set to either 2 or 3 throughout the entire operating range of 22.5–26.5 V, with level 1 reserved solely for low illumination (such as indoor) conditions. In this setup, pixel-wise range-gating is evaluated through range measurements up to 54 m, as summarized in Table 1. Figure 15 shows measurement results at various distances, with success rate defined as the percentage of correct ToF measurements after a 50-ms integration period (equivalent to 20-fps imaging). The system operates in flash illumination mode, where the laser illuminates the entire scene, and a representative histogram from a single pixel is shown. Using 90% success-rate threshold, the method extends the maximum measurable range by 1.7× while providing 7.1-dB improvement in histogram SNR. Additionally, range gating effectively suppresses pile-up distortion by confining the histogram to a narrower time window and substantially reduces the total number of recorded events, minimizing the required memory for histogram storage. Since these measurements emulate

a 20-fps flash imaging scenario, it is evident that the proposed pixel-wise range gating technique improves the sensor's maximum range, while maintaining the proper frame rate required in automotive applications.

3.4 SETUP3 Measurement Results

This setup evaluates the sensor's range-finding performance under high background illumination and long-range conditions (up to 100 m), representative of demanding daytime automotive scenarios. Due to limitations in the measurement setup, interference test using time-coded TCSPC is not conducted in this setup. However, according to the analysis provided in Section 2.1, time-coded TCSPC is theoretically independent of measurement range. Furthermore, interference test results in SETUP1 and SETUP2 (Figure 11 and Figure 14) demonstrate that the interference suppression provided by the time-coded TCSPC method in these setups at approximately 5-m and 23-m distances are 15.85 dB and 15.95 dB, respectively, which confirms the independence of this method on the measurement range. Since interference suppression was validated in previous setups and modeled through the proposed time-coded TCSPC technique, this experiment primarily focuses on sensor operation under extreme background noise. Accordingly, the time-coded TCSPC is disabled, and standard TCSPC processing is used to generate the final histograms.

The supply voltage thresholds for adaptive coincidence detection are set to 22.5 V and 23.3 V, lower than in earlier setups due to stronger background noise. The SPAD supply voltage is set to 23.6 V to enable the highest level of coincidence detection and maximize noise suppression. If the voltage drops to 23.3 V, the coincidence threshold automatically decreases by one level to maintain sufficient signal detection, ensuring high noise immunity with minimal sensitivity to supply variations. Range gating is also enabled, though applied globally (not pixel-wise) since this is a single-point measurement. The gating follows the logic in Table 1, with events beyond the range window of 60–100 m grouped into a single wide window. Because the noise profile typically decreases at longer ranges due to the limited sensor throughput and pile-up effect, this broader gating window remains effective.

Figure 16 shows a sample histogram for a highly reflective target at 90 m, with and without range gating. Without gating, strong background noise and pile-up distortion obscure the weak long-range return, making ToF extraction unreliable. With gating enabled, event detection is

focused on the window of 60–100 m, and most noise and pile-up artifacts are suppressed, significantly improving SNR and enabling accurate and stable ToF measurement.

Figure 17 shows the success rate of single-point measurements at varying distances up to 100 m with a 50-ms integration. Without range gating, sensor performance degrades beyond 80 m, with success rate dropping to approximately 65% at 100 m. With range gating enabled, however, the success rate exceeds 90% at 100 m, demonstrating reliable operation under 103-klux background illumination and confirming effective long-range performance in high-noise conditions.

4. Discussion

The combined implementation of time-coded TCSPC, adaptive coincidence detection, and pixel-wise range gating establishes a holistic framework that enhances robustness of SPAD-based d-ToF LiDARs in dense urban automotive environments. Together, they address three primary limitations, ambient light noise, inter-LiDAR interference, and voltage- or scene-dependent sensitivity, without compromising frame rate, photon efficiency, or scalability.

System-level results demonstrate reliable operation under illumination exceeding 100 klux (bright daylight) without complex optical filtering or power-intensive modulation. Unlike earlier TCSPC- or gating-based approaches that trade SNR for reduced frame rate or range, the proposed methods preserve real-time imaging while improving SNR and interference immunity through intelligent timing and adaptive circuit techniques rather than brute-force optical or computational filtering.

Compared to fixed-gate and fixed-threshold SPAD systems, adaptive coincidence detection decouples DCR sensitivity from operating voltage, ensuring stable photon detection across wide bias and temperature variations, critical for large automotive SPAD arrays. Pixel-wise range gating provides localized, depth-adaptive temporal filtering, overcoming limitations of fixed-gate designs. Its integration with TCSPC enables selective histogram accumulation, improving SNR and memory efficiency for scalable, high-frame-rate 3D imaging.

Time-coded TCSPC enhances resilience to multi-LiDAR interference, increasingly problematic in dense urban environments with multiple 905-nm systems. Unlike correlation-based or PPM schemes that require multiple pulses and reduce eye-safe range or frame rate, this method embeds pseudo-random timing signatures within a single pulse per cycle by modulating laser repetition rate. This preserves optical power and real-time operation while statistically dispersing

interference in the histogram, achieving code-domain mitigation with minimal hardware overhead and no photon-throughput penalty.

Together, these techniques form a hierarchical suppression strategy:

• Temporal coding mitigates coherent interference.

• Adaptive coincidence detection stabilizes sensitivity against voltage and dark-count variations while suppressing noise.

• Pixel-wise range gating filters asynchronous and out-of-range noise and interference.

This multi-layered approach fundamentally differs from prior art, providing resilience across illumination levels, target distances, and environmental dynamics without degrading core sensor specifications.

Table 2 compares the proposed system with state-of-the-art d-ToF LiDARs. The prototype sensor, powered by combined application of the three proposed techniques, achieves the longest distance measurement and enables 3D imaging at frame rates and background light levels required for automotive applications. Furthermore, it features a fully solid-state architecture with flash illumination and SPAD detection. This performance is superior to that of traditional implementations listed in Table 2, which fail to achieve either single-point measurement or 3D imaging at comparable distances under the required frame rate and background light conditions.

Overall, the measured results position the system as a bridge between research-grade SPAD imagers and automotive-ready LiDARs. By shifting suppression complexity from optics to electronics, the architecture enables compact, monolithically-integrated LiDAR frontends without mechanical scanning or extensive external filtering. Since the techniques rely on generic timing and control logic, they are compatible with emerging 3D-stacked SPAD arrays and digital photon counters, providing a scalable, power-efficient foundation for next-generation LiDAR-on-chip systems.

In summary, integration of adaptive circuit techniques and temporal coding defines a new operating regime for SPAD-based d-ToF LiDAR, simultaneously optimizing noise resilience, range, and imaging speed to meet the stringent demands of autonomous driving in complex urban environments.

5. Conclusions

In this paper, we presented a SPAD-based d-ToF LiDAR architecture that integrates three novel techniques for robust, high-speed, and noise- and interference-resilient operation under varying illumination conditions. The main conclusions are:

• Time-coded TCSPC mitigates inter-LiDAR interference while maintaining full frame rate and photon efficiency in dense automotive environments.

• Adaptive coincidence detection compensates for supply-voltage-dependent DCR variations, ensuring stable operation across a wide bias range.

• Pixel-wise range gating suppresses out-of-range noise and pile-up, improving histogram SNR while reducing memory and processing overhead.

• The combined methods form a unified, CMOS-compatible framework for noise and interference suppression in SPAD-based d-ToF sensors.

• Measurements demonstrate 20-fps imaging up to 34 m under 79-klux background illumination, and accurate single-point detection up to 100 m with over 90% success rate under 103-klux background illumination, confirming reliable daytime performance.

• The architecture is scalable to large SPAD arrays and suitable for compact, high-speed LiDARs for autonomous and assisted driving applications.

Overall, the proposed techniques provide a power-efficient, scalable foundation for next-generation automotive LiDARs, bridging the gap between research prototypes and automotive-ready implementations.

References

1. Niclass, C., Soga, M., Matsubara, H., et al. "A 100-m range 10-Frame/s 340×96-pixel time-of-flight depth sensor in 0.18-µm CMOS," *IEEE Journal of Solid-State Circuits*, **48**(2), pp. 559-572 (2013). https://doi.org/10.1109/JSSC.2012.2227607

2. Yoshioka, K., Kubota, H., Fukushima, T., et al. "A 20-ch TDC/ADC hybrid architecture LiDAR SoC for 240×96 pixel 200-m range imaging with smart accumulation technique and residue quantizing SAR ADC," *IEEE Journal of Solid-State Circuits*, **53**(11), pp. 3026-3038 (2018). https://doi.org/10.1109/JSSC.2018.2868315

3. Li, Y. and Ibanez-Guzman, J., "Lidar for autonomous driving: the principles, challenges, and trends for automotive Lidar and perception systems," *IEEE Signal Processing Magazine*, **37**(4), pp. 50-61 (2020). https://doi.org/10.1109/MSP.2020.2973615

4. Morrison, D., Kennedy, S., Delic, D., et al. "A 64×64 SPAD flash LIDAR sensor using a triple integration timing technique with 1.95 mm depth resolution," *IEEE Sensors Journal*, **21**(10), pp. 11361-11373 (2021). https://doi.org/10.1109/JSEN.2020.3030788

5. Jami, S. T., Dabidian, S., Kavehvash, Z., et al. "Noise and interference co-suppression technique in SPAD-based direct time-of-flight (d-ToF) pulsed LiDAR sensors," *2025 IEEE SENSORS*, Vancouver, BC, Canada, pp. 1-4 (2025). https://doi.org/10.1109/SENSORS59705.2025.11331064

6. Villa, F., Severini, F., Madonini, F., et al. "SPADs and SiPMs arrays for long-range high-speed light detection and ranging (LiDAR)," *Sensors*, **21**(11), 3839 (2021). https://doi.org/10.3390/s21113839

7. Chen, G., Wiede, C. and Kokozinski, R. "Data processing approaches on SPAD-based d-TOF LiDAR systems: a review," *IEEE Sensors Journal*, **21**(5), pp. 5656-5667 (2021). https://doi.org/10.1109/JSEN.2020.3038487

8. Incoronato, A., Locatelli, M. and Zappa, F. "Statistical modelling of SPADs for time-of-flight LiDAR," *Sensors*, **21**(13), 4481 (2021). https://doi.org/10.3390/s21134481

9. Feng, L., Liu, Y., Li, D., et al. "Robust compressive histogramming based on autoencoder for SPAD direct ToF LiDAR covering challenging scenarios," *IEEE Sensors Journal*, **25**(14), pp. 27701-27711 (2025). https://doi.org/10.1109/JSEN.2025.3575784

10. Padmanabhan, P., Zhang, C. and Charbon, E. "Modeling and analysis of a direct time-of-flight sensor architecture for LiDAR applications," *Sensors*, **19**(24), 5464 (2019). https://doi.org/10.3390/s19245464

11. Dai, Z., Wolf, A., Ley, P. -P., et al. "Requirements for automotive LiDAR systems," *Sensors*, **22**(19), 7532 (2022). https://doi.org/10.3390/s22197532

12. Kashmiri, M., Behroozpour, B., Petkov, V. P., et al. "A 4-GS/s 80-dB DR current-domain analog frontend for phase-coded pulse-compression direct time-of-flight automotive lidar," *IEEE Journal of Solid-State Circuits*, **55**(12), pp. 3131-3145 (2020). https://doi.org/10.1109/JSSC.2020.3022658

13. Grollius, S., Grosse, S., Ligges M., et al. "Optimized interference suppression for TCSPC LiDAR," *IEEE Sensors Journal*, **22**(24), pp. 24094-24101 (2022). https://doi.org/10.1109/JSEN.2022.3216810

14. Zhu, G., Nan, Z., Zhang, X., et al. "High anti-interference 3D imaging LIDAR system based on digital chaotic pulse position modulation," *Optics & Laser Technology*, **163**, 109405 (2023). https://doi.org/10.1016/j.optlastec.2023.109405

15. Seo, H., Yoon, H., Kim, D., et al. "Direct TOF scanning LiDAR sensor with two-step multievent histogramming TDC and embedded interference filter," *IEEE Journal of Solid-State Circuits*, **56**(4), pp. 1022-1035 (2021). https://doi.org/10.1109/JSSC.2020.3048074

16. Ruokamo, H., Hallman L. W. and Kostamovaara, J. "An 80×25 pixel CMOS single-photon sensor with flexible on-chip time gating of 40 subarrays for solid-state 3-D range imaging," *IEEE Journal of Solid-State Circuits*, **54**(2), pp. 501-510 (2019). https://doi.org/10.1109/JSSC.2018.2878816

17. Padmanabhan, P., Zhang, C., Cazzaniga, M., et al. "A 256×128 3D-stacked (45nm) SPAD FLASH LiDAR with 7-level coincidence detection and progressive gating for 100m range and 10klux background light," *2021 IEEE International Solid-State Circuits Conference (ISSCC)*, San Francisco, CA, USA, pp. 111-113 (2021). https://doi.org/10.1109/ISSCC42613.2021.9366010

18. Dabidian, S., Tafaghodi Jami, S., Kavehvash, Z., et al. "Direct time-of-flight (d-ToF) pulsed LiDAR sensor with simultaneous noise and interference suppression," *IEEE Sensors Journal*, **24**(17), pp. 27578-27586 (2024). https://doi.org/10.1109/JSEN.2024.3425173

19. Manuzzato, E., Tontini, A., Seljak A., et al. "A 64×64-pixel flash LiDAR SPAD imager with distributed pixel-to-pixel correlation for background rejection, tunable automatic pixel sensitivity and first-last event detection strategies for space applications," *2022 IEEE International Solid-State Circuits Conference (ISSCC)*, San Francisco, CA, USA, pp. 96-98 (2022). https://doi.org/10.1109/ISSCC42614.2022.9731622

20. Hu, J., Li, D., Wang, X., et al. "A 64-channel SPAD-based LiDAR sensor with compact coincidence detection circuit and interframe correlation-based nonlinear partial histogram builder," *2024 IEEE Asian Solid-State Circuits Conference (A-SSCC)*, Hiroshima, Japan, pp. 1-3 (2024). https://doi.org/10.1109/A-SSCC60305.2024.10849217

21. Gyongy, I., Dutton, N. A. W. and Henderson, R. K. "Direct time-of-flight single-photon imaging," *IEEE Transactions on Electron Devices*, **69**(6), pp. 2794-2805 (2022). https://doi.org/10.1109/TED.2021.3131430

22. Tontini, A., Gasparini, L. and Perenzoni, M. "Numerical model of SPAD-based direct time-of-flight flash LIDAR CMOS image sensors," *Sensors*, **20**(18), 5203 (2020). https://doi.org/10.3390/s20185203

23. Zhuo, S., Xia, T., Zhao, L., et al. “Solid-state dToF LiDAR system using an eight-channel addressable, 20-W/Ch transmitter, and a 128×128 SPAD receiver with SNR-based pixel binning and resolution upscaling,” *IEEE Journal of Solid-State Circuits*, **58**(3), pp. 757-770 (2023). https://doi.org/10.1109/JSSC.2022.3227078

24. Kim, B., Park, S., Han, S. -H., et al. “A CMOS flash LiDAR sensor with in-pixel zoom histogramming time-to-digital converters,” *IEEE Journal of Solid-State Circuits*, **60**(4), pp. 1449-1460 (2025). https://doi.org/10.1109/JSSC.2024.3508614

25. Feng, L., Liu, Y., Li, D., et al. “Robust compressive histogramming based on autoencoder for SPAD direct ToF LiDAR covering challenging scenarios,” *IEEE Sensors Journal*, **25**(14), pp. 27701-27711 (2025). https://doi.org/10.1109/JSEN.2025.3575784

List of Captions

Figure 1: Time-Coded TCSPC. PLD: Pulsed Laser Diode, BGL: Background Light.

Figure 2: Depth Imaging using Time-Coded TCSPC.

Figure 3: Time-coded TCSPC Simulation. BGL: Background Light.

Figure 4: Adaptive Coincidence Detection.

Figure 5: Pixel-Wise Range Gating.

Figure 6: Pixel-Wise Range Gating Circuit. RG: Range Gating.

Figure 7: Range Gating Simulation.

Figure 8: LiDAR Measurement Setup Block Diagram. PLD: Pulsed Laser Diode, BGL: Background Light, BPF: Bandpass Filter.

Figure 9: Indoor Measurement Setup “SETUP1”. PLD: Pulsed Laser Diode, BPF: Bandpass Filter.

Figure 10: Outdoor Measurement Setups “SETUP2” and “SETUP3”.

Figure 11: Time-Coded TCSPC in SETUP1.

Figure 12: SETUP1 Depth Imaging.

Figure 13: Adaptive Coincidence Detection in SETUP1. ACD: Adaptive Coincidence Detection.

Figure 14: Time-Coded TCSPC in SETUP2.

Figure 15: Pixel-Wise Range Gating in SETUP2. RG: Range Gating.

Figures and Tables

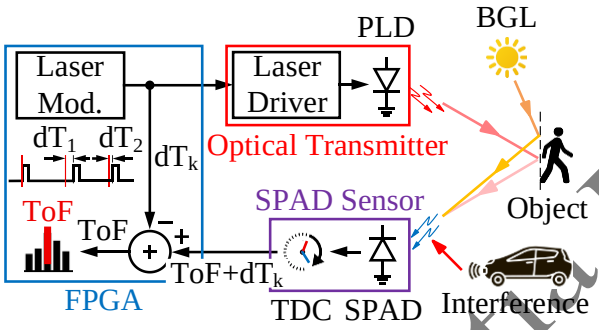

Figure 1

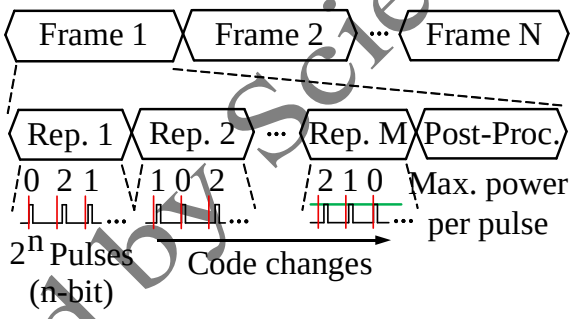

Figure 2

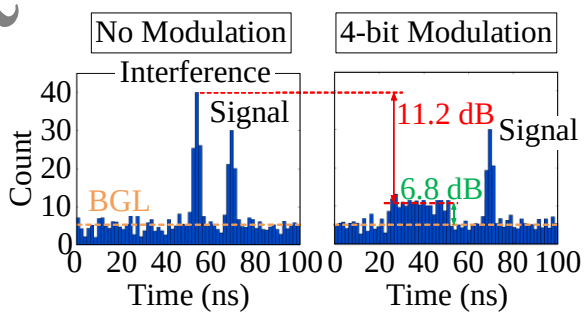

Figure 3

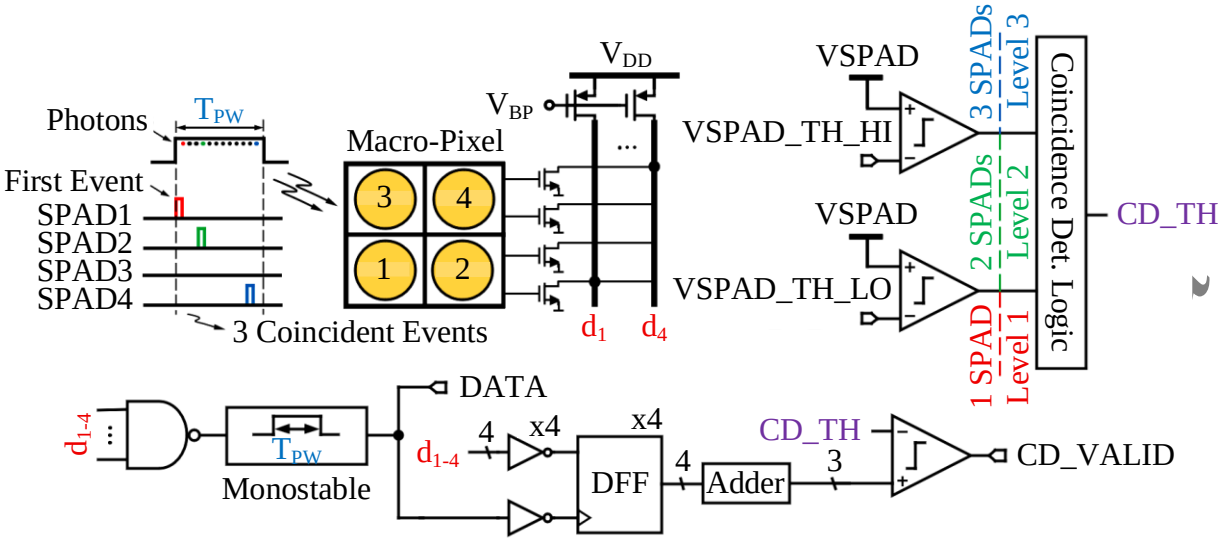

642

643 Figure 4

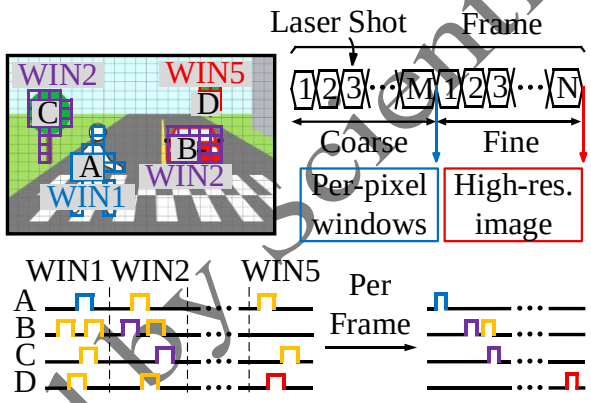

644

645 Figure 5

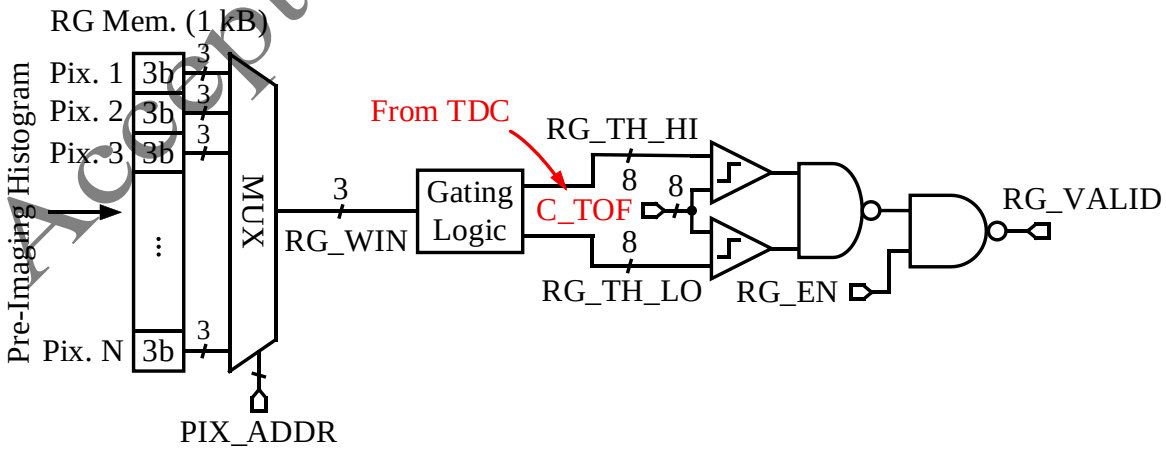

646

647 Figure 6

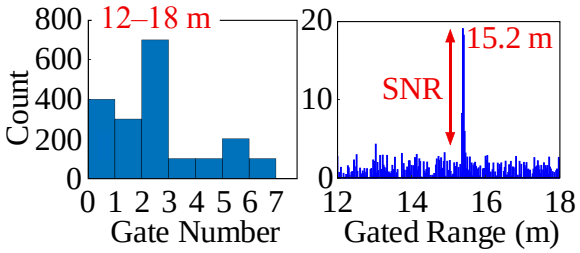

Figure 7

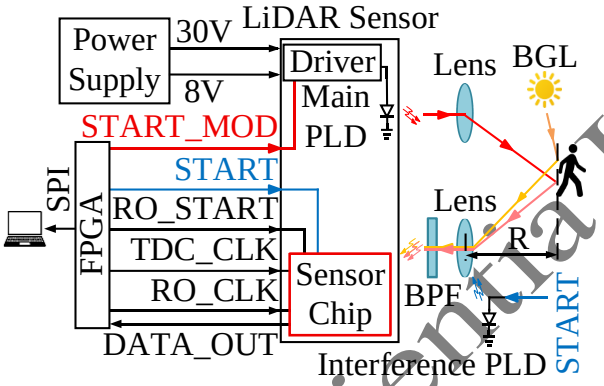

Figure 8

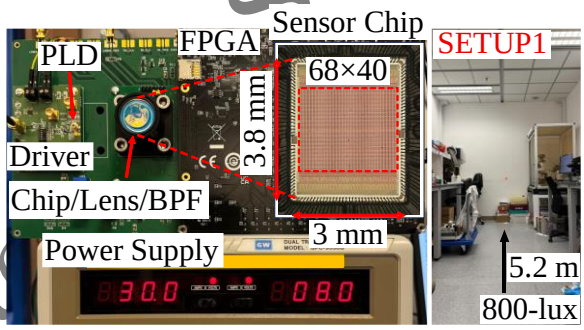

Figure 9

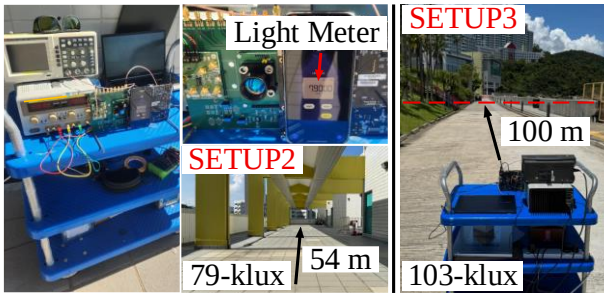

Figure 10

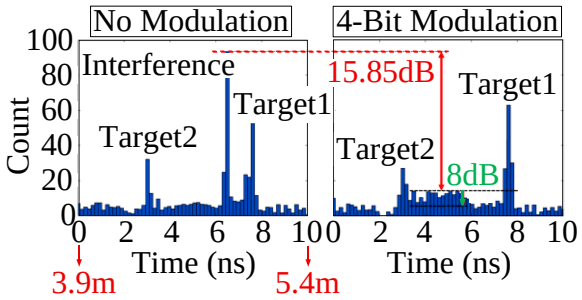

Figure 11

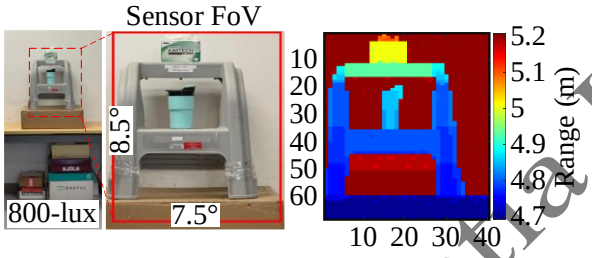

Figure 12

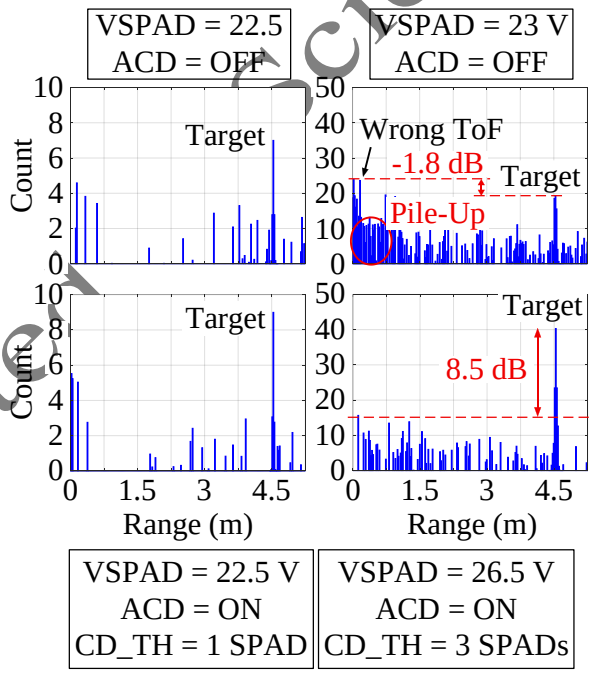

Figure 13

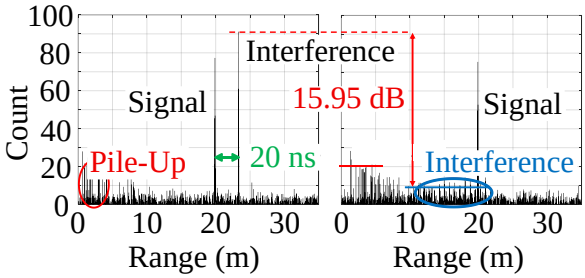

Figure 14

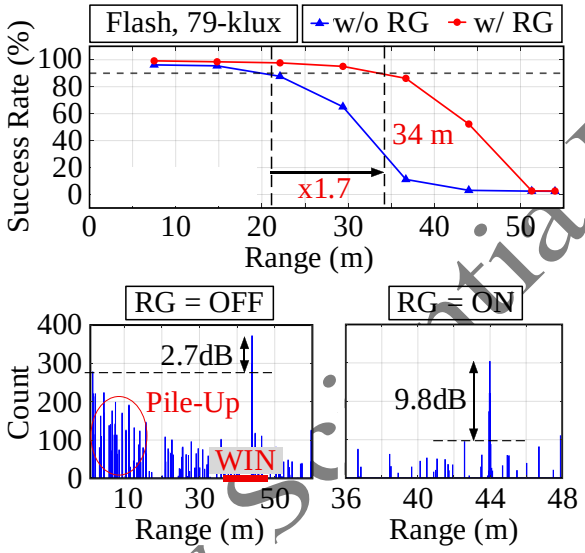

Figure 15

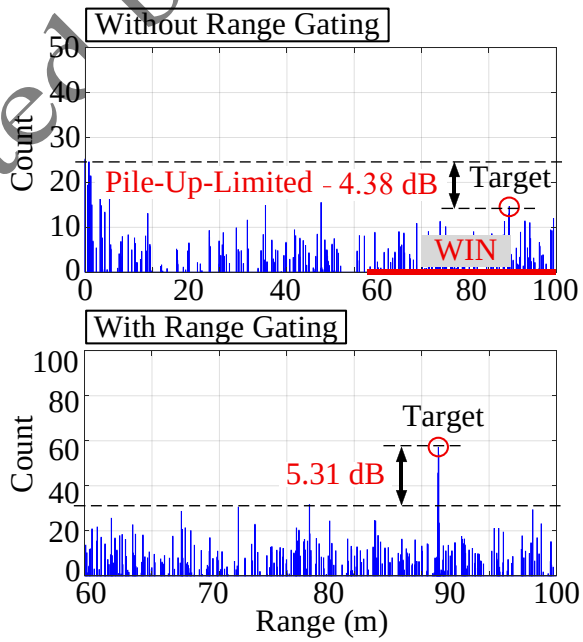

Figure 16

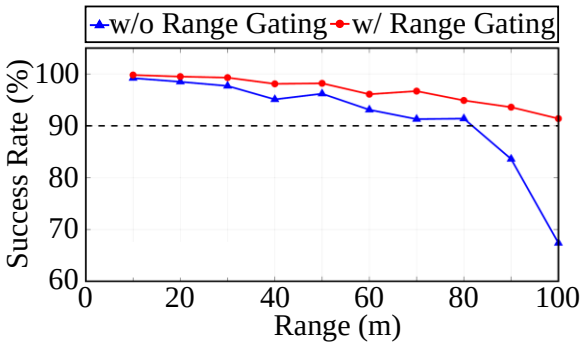

668

669 Figure 17

670 Table 1

RG_WIN	Range (m)	RG_TH_LO	RG_TH_HI
000	0 – 6	00000000	00000100
001	6 – 12	00000100	00001000
010	12 – 18	00001000	00001100
011	18 – 24	00001100	00010000
100	24 – 30	00010000	00010100
101	30 – 36	00010100	00011000
110	36 – 48	00011000	00100000
111	48 – 60	00100000	00111100

671 Table 2

Parameter	Zhuo et al. [23]	Dabidian et al. [18]	Kim et al. [24]	Feng et al. [25]	This Work
Technology	180 nm	Discrete	110 nm	Discrete	180 nm
Pixel Res.	128×128	60×8	100×76	32×32	68×40
Illumination	Hybrid	Scanning	Flash	Flash	Flash
Detection	SPAD	Linear	SPAD	SPAD	SPAD
Noise Suppression	SNR-Based Pixel Binning	Coded TCSPC	TCSPC with Zoom Hist.	TCSPC with Compressive Hist.	1. Coded TCSPC 2. Adapt. Coinc. Det. 3. Pixel-Wise Gating
Interference Suppression	No	Coded TCSPC	No	Autoencoded Hist.	Coded TCSPC
Depth Res. (mm)	15	N/A	90	N/A	23.4
Max. Range (m)	15	4.5	50 (Telemetry) 10 (Imaging)	14	100 (Telemetry) 34 (Imaging)
Frame Rate (fps)	1	2	10	30	20
BGL (klux)	0.5 (Indoor)	Indoor	40	Indoor	103 (Telemetry) 79 (Imaging)

Biographies

Sadra Tafaghodi Jami was born in Mashhad, Iran, in 1995. He received the B.S. degree in electrical engineering and the M.S. degree in microelectronics from Sharif University of Technology, Tehran, Iran, in 2017 and 2019, respectively. He is currently pursuing the dual Ph.D. degree in electronics at Sharif University of Technology, Tehran, Iran, and the Hong Kong University of Science and Technology, Hong Kong. His Ph.D. thesis concerns SPAD-based d-ToF sensors for LiDAR. His current research interests include analog/mixed-signal integrated circuits, pulsed ToF techniques, and SPAD-based sensors.

Ali Fotowat-Ahmady was born in Tehran, Iran, in 1958. He received the B.S. degree from California Institute of Technology, Pasadena, CA, USA, in 1980, and the M.S. and Ph.D. degrees in electrical engineering from Stanford University, Stanford, CA, USA, in 1982 and 1991, respectively. He started his career at Philips Semiconductor, Sunnyvale, CA, USA, in 1987, where he developed several integrated circuits for mobile phones. Since 1991, he has been with the Department of Electrical Engineering, Sharif University of Technology, Iran, where he is an Associate Professor.

Jie Yuan received the B.S. degree in electrical engineering from Tsinghua University in 2000 and the Ph.D. degree in electrical engineering from the University of Pennsylvania, Philadelphia, PA, USA, in 2006. Since 2006, he has been a Faculty Member with the Electronic and Computer Engineering Department, The Hong Kong University of Science and Technology, Hong Kong, where he is currently a Professor. He is currently serving as a Post-Graduate Coordinator with the ECE Department and is in charge of the postgraduate affairs in the ECE Department. His research expertise is on sensory IC design. His research group has made major contributions to the fields of analog-to-digital converter (ADC), CMOS imaging sensors, integrated biocellular sensing systems, wearable sensors, and energy harvesting.